Brain Structure and Function (2019) 224:949–960
https://doi.org/10.1007/s00429-018-1804-0

METHODS PAPER

# High-resolution imaging of distinct human corpus callosum microstructure and topography of structural connectivity to cortices at high field

**Byeong-Yeul Lee[1] · Xiao-Hong Zhu[1] · Xiufeng Li[1] · Wei Chen[1]**

Received: 27 July 2018 / Accepted: 25 November 2018 / Published online: 3 December 2018


## Abstract

Characterization of the microstructural properties and topography of the human corpus callosum (CC) is key to understanding interhemispheric neural communication and brain function. In this work, we tested the hypothesis that high-resolution $T_1$ relaxometry at high field has adequate sensitivity and specificity for characterizing microstructural properties of the human CC, and elucidating the structural connectivity of the callosal fibers to the cortices of origin. The high-resolution parametric $T_1$ images acquired from healthy subjects ($N = 16$) at 7 T clearly showed a consistent $T_1$ distribution among individuals with substantial variation along the human CC axis, which is highly similar to the spatial patterns of myelin density and myelinated axon size based on the histology study. Compared to the anterior part of the CC, the posterior midbody and splenium had significantly higher $T_1$ values. In conjunction with $T_1$-based classification method, the splenial $T_1$ values were decoded more reliably compared to a conventional partitioning method, showing a much higher $T_1$ value in the inferior splenium than in the middle/superior splenium. Moreover, the $T_1$ profile of the callosal subdivision represented the topology of the fiber connectivity to the projected cortical regions: the fibers in the posterior midbody and inferior splenium with a higher $T_1$ (inferring a larger axon size) were mainly connected to motor–sensory and visual cortical areas, respectively; in contrast, the fibers in the anterior/posterior CC with a lower $T_1$ (inferring a smaller axon size) were primarily connected to the frontal/parietal–temporal areas. These findings indicate that high-resolution $T_1$ relaxometry imaging could provide a complementary and robust neuroimaging tool, useful for exploring the complex tissue properties and topographic organization of the human corpus callosum.

**Keywords** Parametric $T_1$ MRI · Corpus callosum · Myelin density · Axon size · Structural connectivity · Topography

## Introduction

The corpus callosum (CC) has the largest abundance of white matter fiber tracts connecting human homologous cortical regions across two hemispheres. It contains more than 200 million fibers and numerous axonal projections essential to interhemispheric communication that is facilitated by the unique structure of myelinated axonal fibers enabling rapid and effective neural signaling and computation (Budd and Kisvarday 2012). Thus, non-invasive imaging and characterization of microstructural architectures and topographical organizations of the callosal subdivisions in human brains is of the utmost importance for providing new insights about interhemispheric structural connectivity and brain function (Myers 1959; Payne 1990; Wahl et al. 2007; Kontis et al. 2009; Sisti et al. 2012).

Quantitative analysis of the CC microstructures has relied on the transmission electron microscopy (TEM) as a gold standard method owing to its superior sensitivity and spatial resolution that make delineating the complex properties of myelinated callosal fibers with great precision and details possible. A number of microscopic studies have shown large variations in myelin density and myelinated axon size between the callosal subdivisions in the postmortem human brain (Aboitiz et al. 1992a, b; Aboitiz and Montiel 2003) and

✉ Byeong-Yeul Lee
bylee@umn.edu

✉ Wei Chen
wei@cmrr.umn.edu

[1] Center for Magnetic Resonance Research, Department of Radiology, University of Minnesota Medical School, 2021 Sixth Street SE, Minneapolis, MN 55455, USA

non-human brain (Stikov et al. 2015b; Lamantia and Rakic 1990; Caminiti et al. 2009, 2013; Innocenti et al. 2010). However, TEM is not applicable for intact brain or longitudinal in vivo studies.

The advent of non-invasive MRI techniques has opened up opportunities for exploring the organization and microstructural properties of the cerebral white matter tissue in vivo (Le Bihan et al. 1986; Chenevert et al. 1990). Diffusion-based imaging methods have been used to explore callosal microstructural properties such as axon diameter and myelin thickness or contents (Assaf et al. 2008, 2013; Caminiti et al. 2013; Zhang et al. 2011; Alexander et al. 2010; Tuch et al. 2002; Fabri et al. 2014; Hofer and Frahm 2006; Stikov et al. 2011, 2015a; Jensen et al. 2005; Callaghan et al. 1988). The topographic information regarding the structural connectivity of callosal fibers to cortical origins has also been documented using the direct injection of axonal tracers in primate brains (Tomasi et al. 2012; Innocenti et al. 2010).

As for non-invasive approaches, there are already several geometric partitioning methods such as Witelson's classification that have been introduced to subdivide the CC structure in the human (Witelson 1989; de Lacoste et al. 1985). Recently, diffusion tensor tractography (DTT)-based approaches have been developed to study the callosal topography (Hofer and Frahm 2006; Huang et al. 2005; Park et al. 2008; Saenz and Fine 2010). However, there have been a lack of high-resolution MRI data linking the unique spatial distribution of callosal microarchitecture to the structural connectivity with a fine spatial scale.

As one of the non-invasive and measurable magnetic resonance (MR) parameters, the longitudinal relaxation time ($T_1$) or rate ($R_1 = 1/T_1$) has been commonly employed for brain research and clinical diagnosis due to the enhanced MRI tissue contrast and sensitivity to tissue environments such as myeloarchitectonics (Sereno et al. 2013; Sigalovsky et al. 2006). Although there is some evidence showing $T_1$ variations of the human CC in some extent (Hofer et al. 2015; Harkins et al. 2016; Wang et al. 2016), the relatively lower spatial resolution is a limiting factor for precise assessment of the fiber microstructural properties and its relevance to the topography of human CC.

In line with our previous report (Lee et al. 2014), in this work, we aimed to test the following hypotheses: (1) high-resolution $T_1$ relaxometry at high field could offer reliable assessment about microstructural properties of the CC and their variations in individual healthy human subjects; (2) the callosal $T_1$ variations would be a sensitive measure to link the key features of the myelin density and myelinated axon diameter; and (3) $T_1$ variations among the callosal subdivisions would be indicative of topography of the callosal fibers in relevance to cortical regions of origin. To test these hypotheses, high-resolution ($0.5 \times 0.5 \times 1$ mm$^3$ voxel size) parametric $T_1$ images of the human corpus callosum were acquired at a high magnetic field of 7 Tesla (T) to assess microstructure properties of the human CC with a minimal partial volume effect. Furthermore, we examined the relation between the $T_1$ variation of the CC subdivisions and its structural connectivity to the projected cortical regions using diffusion tensor tractography. For the validation of the correlate of the in vivo $T_1$ results with underlying microstructural properties, callosal $T_1$ imaging results were compared to the previous histology results of the postmortem human CC specimen (Aboitiz et al. 1992a; Aboitiz and Montiel 2003).

## Materials and methods

### Subjects

Sixteen healthy subjects (mean age ± SD = 29.9 ± 12.0 years, 11 male/5 female) participated in this study, which was approved by the institutional review board committee of the University of Minnesota. The informed consent was obtained from all participants.

### MR imaging protocols

All MRI studies were conducted using an actively shielded 7.0 T/90 cm whole-body human MRI scanner (MAGNETOM/Siemens, Erlangen, Germany) with a 32-channel $^1$H receive array head coil (Nova Medical, Inc., MA, USA).

A mid-sagittal MRI slice across the central corpus callosum was selected under guidance of three-dimensional high-resolution $T_1$-weighted ($T_1$w) images as demonstrated in Fig. 1, which were acquired with a magnetization-prepared rapid gradient echo imaging sequence (TR/TE/TI = 3000 ms/2.4 ms/1200 ms, radiofrequency (RF) pulse flip angle (FA) = 7°, field of view (FOV) = 256 × 256 mm$^2$, isotropic resolution = 0.8 mm, and GRAPPA parallel imaging acceleration factor = 2).

High-resolution diffusion-weighted images were acquired according to the protocol optimized by the Human Connectome Project (HCP) at 7 T (Vu et al. 2015; Ugurbil et al. 2013) with the following acquisition parameters: TR/TE = 5700 ms/66 ms, FA = 90°, $b$ = 2100 mm$^2$/s, number of diffusion direction = 114, in-plane resolution = 1.25 × 1.25 mm$^2$, slice thickness = 1.25 mm, GRAPPA acceleration factor = 3, and multiband factor = 2 (Moeller et al. 2010). Two diffusion image datasets with reversed phase-encode blips were collected for correcting the susceptibility-induced distortions and then combined into a single corrected one (Andersson et al. 2003); thus, a total of 228 image volumes were acquired.

A magnetization-prepared single-shot fast spin echo imaging sequence was used for the parametric $T_1$ measurement (Li et al. 2015) with the following parameters (TR/

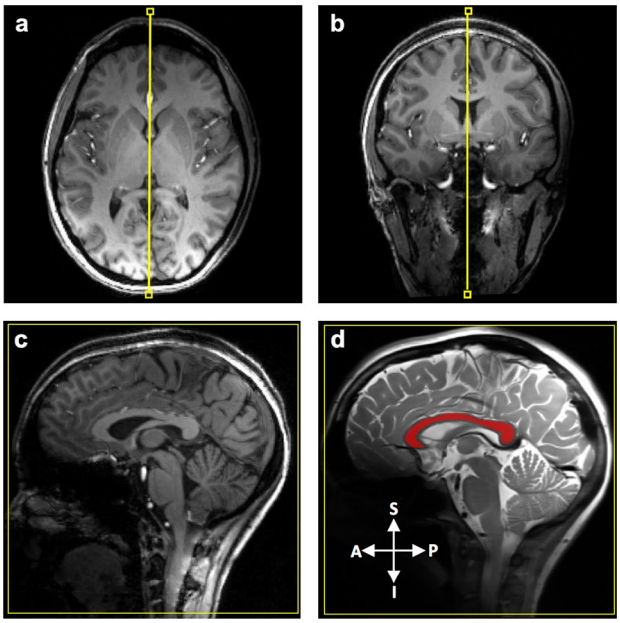


**Fig. 1** A mid-sagittal slice selection of the human corpus callosum using high-resolution three-dimensional $T_1$-weighted images. Each panel of **a**–**c** represents an axial, coronal, and sagittal view, respectively. Panel **d** shows the masked CC (red) displayed on the $T_2$-weighted sagittal image. The arrows shown in **d** represent different anatomical directions; A for anterior, P for posterior, I for inferior, and S for superior

TE = 6000 ms/16 ms, FOV = 192 × 192 mm$^2$, in-plane resolution = 0.5 × 0.5 mm$^2$, slice thickness = 1 mm, GRAPPA acceleration factor = 3 with 24 reference lines, receiver bandwidth (BW) = 814 Hz/pixel, a single mid-sagittal slice image covering the entire CC structure with a perpendicular fiber orientation). Based on the reported $T_1$ value (~ 1.2 s) of the human white matter at 7 T (Rooney et al. 2007; Wright et al. 2008), all $T_1$ images were acquired under a full relaxation condition (TR = 6 s) with various inversion recovery times (TIs) (0.1, 0.15, 0.3, 0.5, 0.8, 1.2, and 1.6 s). The uniform RF pulse flip angles for inversion (FA = 180°) and excitation (FA = 90°) across the selected mid-sagittal CC slice were achieved by applying a slice-selective adiabatic hyperbolic secant pulse (pulse length = 20 ms, BW = 1 kHz) (Garwood and DelaBarre 2001) and variable-rate selective excitation RF pulse (Hargreaves et al. 2004), respectively. The RF transmission power was calibrated using a 2D actual flip-angle imaging (Yarnykh 2007) ($TR_1/TR_2$ = 70 ms/120 ms, TE = 2.5 ms, FOV = 196 × 196 mm$^2$, in-plane resolution = 4 × 4 mm$^2$, and average = 5). All $T_1$ images were collected within 24 min under the FDA-specific absorption rate limit.

## $T_1$ mapping

$T_1$ relaxation maps were generated using the nonlinear least-square fitting algorithm using Matlab software (13.0v, Mathwork) according to the following equation (Li et al. 2015):

$$S(\mathrm{TI}) = \sqrt{\left[S_o\left(1 - 2e^{\left(\frac{-\mathrm{TI}}{T_1}\right)} + e^{\left(\frac{-T_r}{T_1}\right)}\right)\right]^2 + C_{\mathrm{noise}}^2}, \quad (1)$$

where $S$(TI) is the measured imaging signal intensity at a given TI, $S_o$ is the proton density, $T_r$ is the recovery time after the inversion pulse, and $C_{\mathrm{noise}}$ is the noise-related constant.

## $T_1$ distributions of callosal subdivisions

For the regional callosal $T_1$ analysis across subjects, a callosal $T_1$ image of each subject was first registered to a representative subject using a linear affine transformation (Good et al. 2001; Narr et al. 2000).

Using the registered $T_1$ maps, histogram analysis for the $T_1$ distribution of the callosal subdivision was performed; in conjunction with Witelson's classification scheme (Witelson 1989), the CC was parcellated into five vertical partitions based on arithmetic fractions of the maximum anterior–posterior extent: anterior third [rostrum (G1), genu (G2), and rostral body (G3)], anterior midbody (B1), posterior midbody (B2), isthmus (I), and splenium (S). In particular, two partitioning methods were used for further classification of splenial subdivisions—superior (S1), middle (S2), and inferior (S3): an equidistant partitioning method (Aboitiz et al. 1992a; Björnholm et al. 2017; Thapaliya et al. 2017) and $T_1$-based partitioning with a $k$-means method.

## Myelin density and axon diameter

The relation between the callosal $T_1$ variation and the myelinated axon size was examined based on an assumption of a linear relationship between the myelin density (or MWF: myelin water fraction) and $R_1$ (= $1/T_1$).

The in vivo axon diameter map was constructed from the use of $g$-ratio and MWF as a function of axonal diameter ($d_a$). Given the inverse relation between $T_1$ and MWF, the $T_1$ value can be expressed as a function of MWF (or $d_a$) according to the following equations:

$$g\text{-ratio} = \frac{d_a}{d_a + 2t_m}, \quad (2)$$

$$\mathrm{MWF} = \frac{\pi}{4}(1 - \text{g-ratio}^2), \quad (3)$$

$$T_1 \approx \beta/\mathrm{MWF} + \alpha, \quad (4)$$

where $t_m$ is the myelin thickness, and $\alpha$ and $\beta$ are constants. Based on the reported mean value of human axon diameter (0.69 μm) (Liewald et al. 2014) and mean callosal $T_1$

value (1.04 s) as measured in the current study,$\alpha$ and $\beta$ were determined from the regression of Eq. (4). Finally, using the established relation between $T_1$ and MWF in Eq. (4), the axon diameter of each voxel was determined by the corresponding clustered $T_1$ values according to Eqs. (2)–(4), which was classified by the *k*-means method.

For a comparison purpose, another axon diameter map was scaled and constructed using a linear relation between $T_1$ values and axon diameter (Harkins Kevin et al. 2016). The predicted axon diameter for each voxel was determined according to the corresponding clustered $T_1$ values. This map was used for visualization and comparison with the schematic drawing of axon distribution of human CC based on the histology results as reported in the literature.

### Structural connectivity

The relation of $T_1$ variations among CC subdivisions with structural connectivity to the projected cortical regions was investigated using the DTT imaging method. All diffusion data were processed according to the HCP diffusion pipeline (Sotiropoulos et al. 2013) and a probabilistic fiber tractography was applied in subject-specific native space using FSL's FMRIB's Diffusion Toolbox with the following parameters (number of diffusion direction = 3/voxel, number of samples = 5000/voxel, curvature threshold = 0.2, and maximum number of step = 2000, and step length = 0.5 mm). The procedure of the probabilistic tractography is described in detail in the literature (Behrens et al. 2007). Briefly, representative regions of interest (ROIs) were first delineated on the callosal $T_1$ map. Using Bayesian estimation, fiber directions for each ROI were inferred and then the probability of a streamline connection was calculated as the proportion of the total number of streamlines. Seeded fibers were then classified according to their proportional streamline connection probabilities to the target cortical areas. Finally, voxels with a streamline connection probability of $p$ value > 0.01 (50 out of 5000 streamlines) were only used for fiber tracking to reduce statistical errors due to noise.

### Statistical analysis

A statistical comparison for $T_1$ differences between discrete callosal areas was performed using a two-tailed paired *t*-test. The relation between in vivo $1/T_1$ ($=R_1$) profile and histology analysis of fiber density was examined using Pearson correlation analysis. A corrected $p$ value < 0.05 was considered statistically significant after accounting for multiple comparisons using Bonferroni correction if necessary. All statistical analyses were conducted using the IBM SPSS software version 21.0 (IBM Corp., Armonk, NY, USA). All results were presented as mean ± standard deviation (SD).

## Results

### Callosal $T_1$ distribution

The mean of the $T_1$ relaxation time of the entire human CC was 1.04 ± 0.04 s, which was in an agreement with the reported $T_1$ values of the human white matter at 7 T (Wright et al. 2008; Rooney et al. 2007). The $T_1$ relaxometry map showed a clear spatial trend and widespread variation from the anterior to posterior along the CC, which was consistently observed in all subjects (Fig. 2). Histogram analysis shown in Fig. 3 reveals a significant difference in the $T_1$ values between the anterior and posterior CC parts ($p < 0.001$). Higher $T_1$ values were found in the posterior CC areas including the posterior midbody (1.12 ± 0.04 s, Fig. 3B2) and splenium (1.15 ± 0.08 s, Fig. 3S). In contrast, relatively lower $T_1$ values were shown in the anterior CC areas (0.97 ± 0.01 s, Fig. 3G1–G3) and anterior midbody (1.04 ± 0.03 s, Fig. 3B1).

The Witelson's partitioning scheme (Fig. 3d) showed large variations of $T_1$ values (i.e., SD) between three sub-sections of the splenial areas: the superior ($T_1 = 1.08 \pm 0.08$ s, Fig. 3e-S1), the middle ($T_1 = 1.14 \pm 0.08$ s, Fig. 3e-S2), and the inferior area ($T_1 = 1.19 \pm 0.08$ s, Fig. 3e-S3). In contrast, the $T_1$-based clustering method (Fig. 3f) showed large mean $T_1$ differences with a much smaller SD: the superior ($T_1 = 1.08 \pm 0.01$ s, Fig. 3g-S1), the middle ($T_1 = 1.10 \pm 0.02$ s, Fig. 3g-S2), and the inferior area ($T_1 = 1.25 \pm 0.04$ s, Fig. 3g-S3). This method resulted in a better separation of these areas ($\Delta T_1 = 0.17$ s, Fig. 3g) compared to the Witelson's partitioning method ($\Delta T_1 = 0.11$ s, Fig. 3e).

### Callosal fiber composition

There was a strong correlation between the $R_1$ values from MRI measurement (Fig. 4a, b) and the normalized fiber density from histology measurement (Fig. 4e) along the equidistant 10 sectors (Fig. 4d; regression coefficient $R = 0.81$, $p = 0.004$); the lowest $R_1$ value in the posterior midbody (B3) corresponded to the lowest fiber density, whereas the highest $R_1$ in the anterior parts of the CC (G1–G3) corresponded to the highest fiber density. As shown in Fig. 3, $R_1$ in the inferior splenium (S4) was significantly lower than in the middle (S3)/superior (S5) and even lower than in B3, implying the lowest fiber density among the CC subdivisions. Note that compared to the in vivo $T_1$ (Fig. 3a) or $R_1$ (Fig. 4a) imaging analysis, the histology analysis in the literature did not provide full spatial distribution of the fiber density across the entire CC

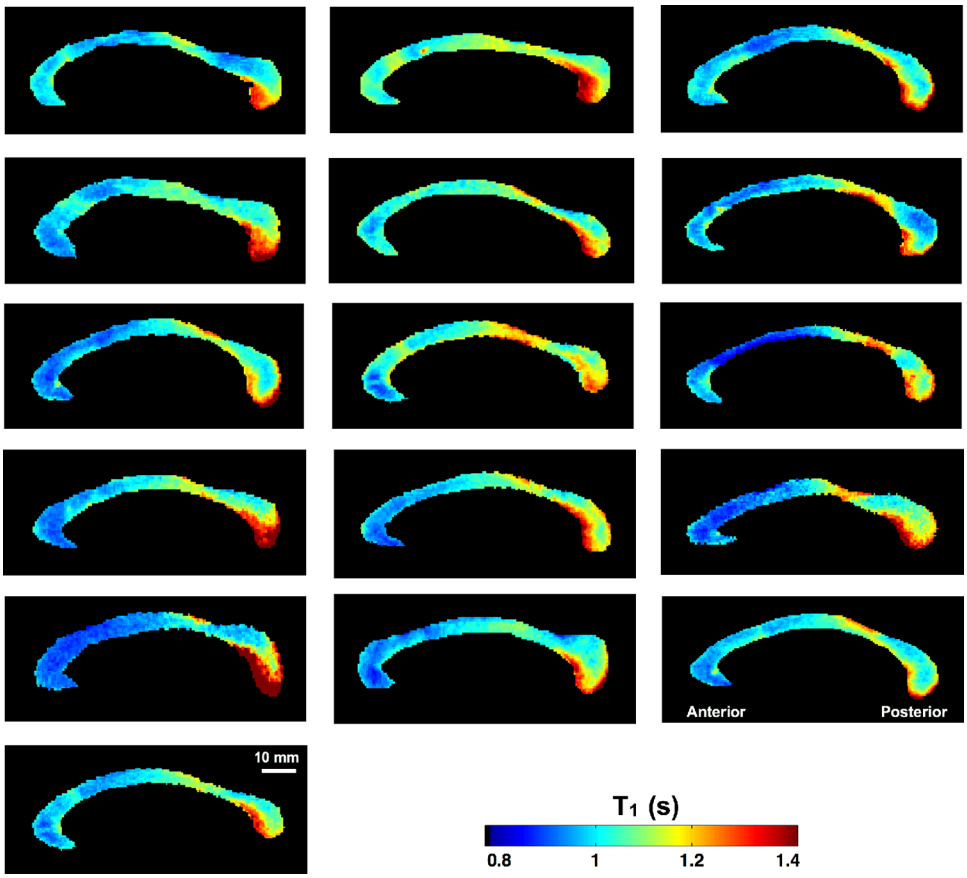


**Fig. 2** High-resolution $T_1$ relaxometry maps of the mid-sagittal corpus callosum from 16 healthy human subjects. All $T_1$ maps were displayed in the same scale in the color bar. There was a common pattern of $T_1$ distributions along the CC; the smaller $T_1$ values in the anterior and higher $T_1$ values toward the posterior areas

structure since only a very small portion of callosal subsections was analyzed for each CC subdivision (Aboitiz et al. 1992a). Interestingly, a recent diffusion study demonstrated the similar distribution of CC axon diameters along the human CC, showing the high density of larger axon size in the inferior splenium as well as the midbody (Genc et al. 2018). Taken together, our results suggest that the high-resolution callosal $R_1$ index or relaxometry map measured at high field may reflect the myelinated fiber density across the entire human CC (Hypothesis 1).

Figure 5b displays the estimated myelinated axon diameter map of the human CC (in a relative scale) based on the in vivo $T_1$ imaging measurement, showing a heterogeneous distribution along the human CC axis. The re-scaled axon diameter map (Fig. 5c) shows a similar pattern with the schematic drawing of axon diameter from the histology study [Fig. 5d taken from the literature (Aboitiz and Montiel 2003)]. The similarity suggests that the callosal $T_1$ variation reflects different sizes of the myelinated axon in the human CC (Hypothesis 2).

### Callosal fiber connectivity

Six representative ROIs were defined (i.e., ROI G-S3 as shown in Fig. 6 from a representative subject) for DTT Fiber tractography based on callosal regional $T_1$ profiles. DTT Fiber tractography analysis showed that the callosal fiber bundles located in the genu with the smallest $T_1$ value (ROI G, $T_1 = 0.98 \pm 0.02$ s) were primarily connected to the prefrontal cortex (Fig. 6a). The fiber bundles from two ROIs located in the posterior midbody of B2 (ROI B2, $T_1 = 1.09 \pm 0.02$ s; ROI B3, $T_1 = 1.13 \pm 0.03$ s) were connected to the primary motor cortex (Fig. 6b) and the somatosensory cortex (Fig. 6c), respectively. The fiber bundles in the superior (ROI S1, $T_1 = 1.07 \pm 0.03$ s) and middle part of the splenium (ROI S2, $T_1 = 1.14 \pm 0.05$ s) were mainly connected to the parietal lobe (Fig. 6d) and temporal lobe (Fig. 6e), respectively. In contrast, the ROI located in the inferior part of splenium with the highest $T_1$ value (ROI S3, $T_1 = 1.31 \pm 0.06$ s) projected the callosal axons to the visual cortex (Fig. 6f). These results support the reasoning that the regional $T_1$ profile of CC could reflect the key topographic features of callosal subdivisions in the human brain (Hypothesis 3).

## Discussion

In this study, we demonstrate that the high-resolution $T_1$ relaxometry at 7 T showed greater sensitivity and specificity for detecting the large degree of $T_1$ heterogeneity of the

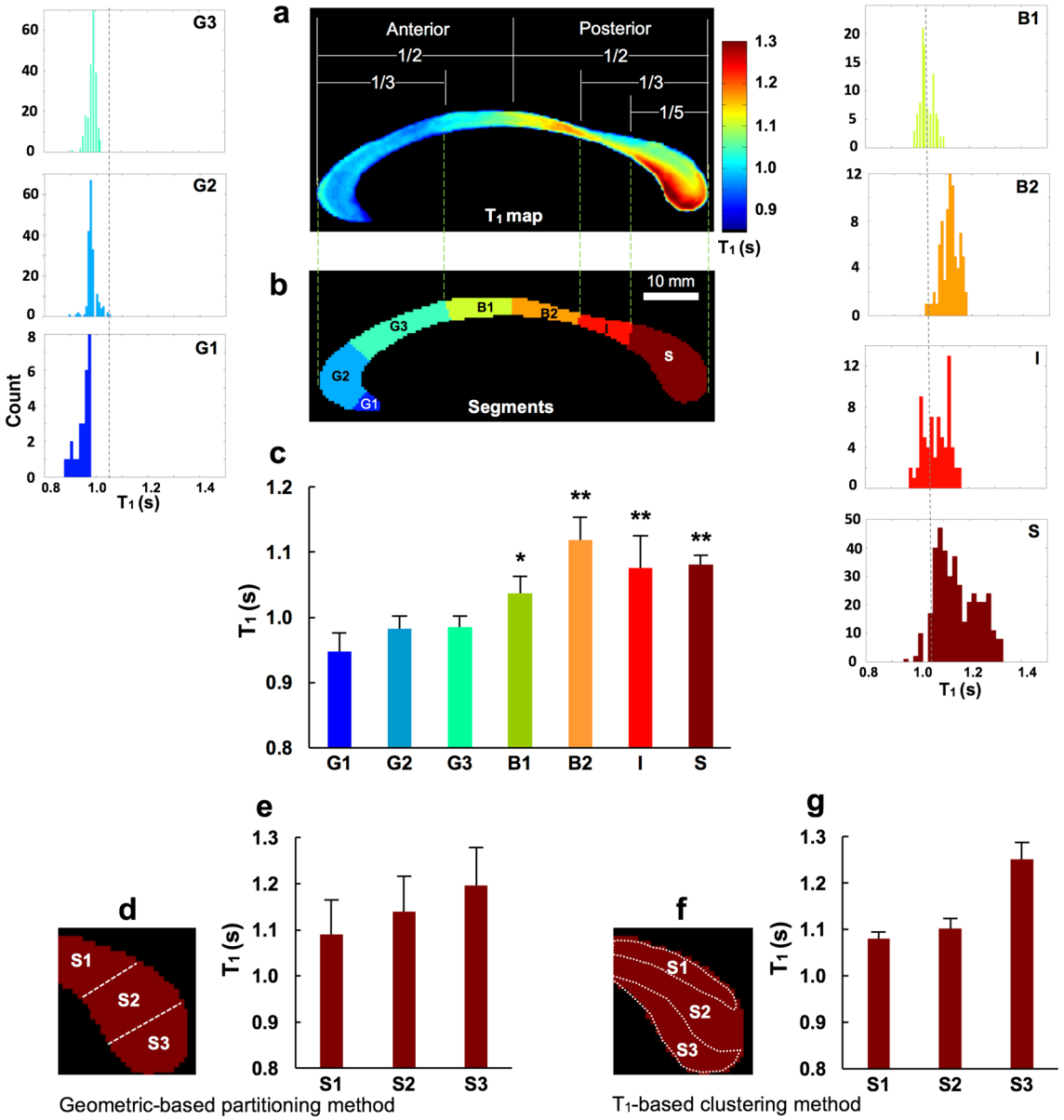


**Fig. 3** Histogram analysis of regional $T_1$ distributions of the callosal subdivisions in conjunction with two partitioning methods. According to the geometric partitioning method, the mid-sagittal corpus callosum was segmented into seven subdivisions: the anterior third including rostrum (G1), genu (G2), rostral body (G3); midbody including anterior midbody (B1) and posterior midbody (B2); posterior-third including the isthmus (I) and splenium (S). The further segmentation for the splenial subdivisions—superior (S1), middle (S2), and inferior (S3)—were performed using the Witelson's partitioning (**d, e**) and $T_1$-based classification method (**f, g**). Overall, $T_1$ map shows a heterogeneous pattern of $T_1$ distribution from the anterior to the posterior part of the CC. Moreover, $T_1$-based classification method provides the better separation of splenial subdivisions compared to the Witelson's method. The vertical dashed lines in the histogram panels indicate the mean $T_1$ value (= 1.04 s) of the entire CC structure. Regional callosal $T_1$ values were compared to mean $T_1$ of the anterior areas (G1–G3) using two-tailed paired *t*-test. $^*p < 0.001$, $^{**}p < 0.0001$

human CC in a fine spatial scale. In addition, such regional $T_1$ variation was relevant to the topographical organization of the fiber connectivity of origin, which was not shown in the previous MR relaxometry studies. Based on a tight correlation of $T_1$ (or $R_1$) to the myelinated axon size and myelin density, the callosal $T_1$ variation may reflect the biological variation, diversity, and structural/functional specialization of the callosal microstructure. Thus, our in vivo results support a key scientific notion: interhemispheric communication for sensorimotor/auditory/visual processing through the CC could be facilitated by the larger-diameter myelinated axons with a faster conduction velocity (Aboitiz et al.

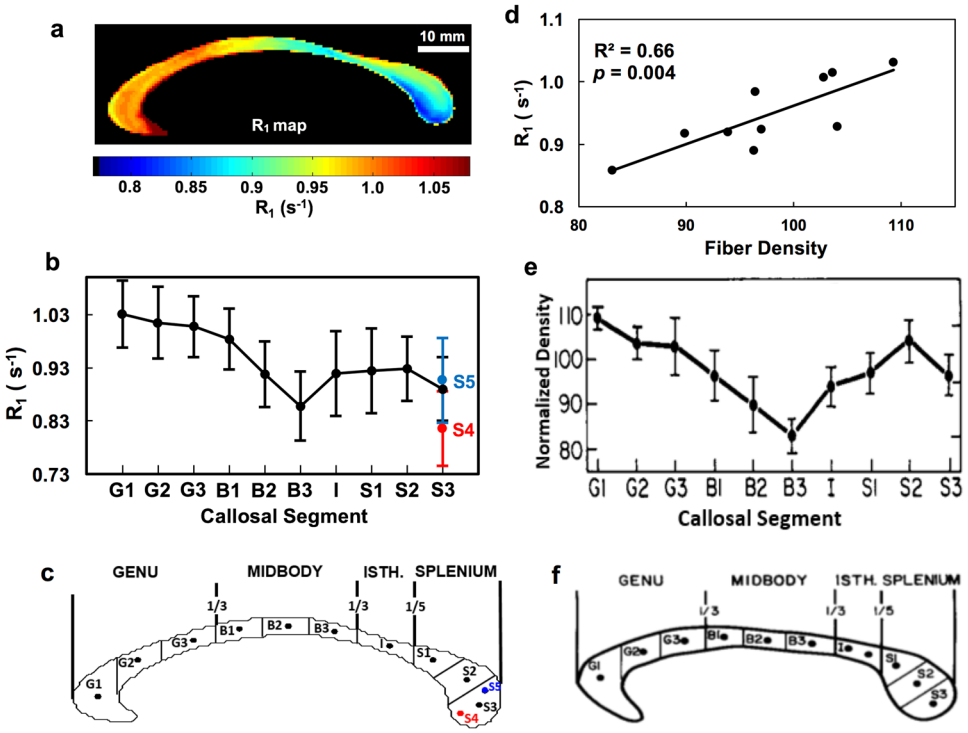


**Fig. 4** Correlation study between in vivo callosal $R_1$ ($=1/T_1$) distribution and myelinated fiber density in the postmortem data. **a** The averaged in vivo $R_1$ relaxometry map of the human CC from all subjects ($n=16$). **b** The in vivo $R_1$ profile along ten equidistant callosal segments: anterior third (G1–G3), midbody (B1–B3), isthmus (I), and splenium (S1–S3) as shown in **c. e** The normalized myelinated fiber density profile. **d** The fiber density shown in panel **e** and in vivo $R_1$ shown in panel **b** show a high correlation along the ten segments. Error bar represents a standard deviation. **e, f** Reprinted with the permission from the reference (Aboitiz et al. 1992a)

1992a; Caminiti et al. 2013), which was associated with a higher $T_1$ value or lower myelin density in the connected CC subdivisions. In contrast, the relatively slower communication between higher-order neural processing cortical areas encompassing the frontal and parietal lobes could be facilitated by relatively higher fiber density and smaller-diameter axons with a low conduction velocity (Berlucchi 1972; Aboitiz and Montiel 2003). Therefore, the high-resolution $T_1$ relaxometry could provide a valuable and robust surrogate reflecting the callosal fiber and axon microarchitecture and neural communication functionality.

To date, several new classification methods for the CC partitions have been proposed to revise the classic viewpoint of human CC topology. For instance, DTT-based parcellation methods have indicated that most fibers in the primary motor cortex were projected toward the posterior midbody of the human CC (Hofer and Frahm 2006). Moreover, fibers from the primary visual cortex were projected toward the inferior part of the splenium (Huang et al. 2005; Putnam et al. 2010; Saenz and Fine 2010). Notably, these findings are strikingly consistent with our observation of regional callosal $T_1$ distributions (Fig. 3) and the concomitant fiber connectivity to the cortex (Fig. 6). Thus, the high-resolution $T_1$ map could be useful as a hallmark underlying topographic organization of the callosal subdivisions. Furthermore, it could provide a feature of the fiber connectivity of individual subjects and account for the inter-subject variability of callosal topography (Aboitiz et al. 1992b; Dougherty et al. 2005a).

Changes in $T_1$ or $R_1$ values in the CC are largely attributed to the degree of the myelinated fiber density or myelin-bound water fraction. $R_1$ relaxivity in the brain tissue can be described as the following (Rooney et al. 2007; Stuber et al. 2014):

$$R_1 \propto R_{1S} + R_{1M} \cdot d_M + R_{1Fe} \cdot [\mathrm{Fe}], \quad (5)$$

where $R_{1S}$ is the relaxivity of a pure saline solution (at physiological temperature) that can be treated as a constant; $R_{1M}$ and $R_{1Fe}$ are the $T_1$ relaxivities of macromolecule and iron, respectively. $d_M$ is the macromolecular density and [Fe] is the iron concentration in the tissue. Since macromolecular composition is rich in the myelin sheath in the human CC tissue, $R_{1M}$ and $d_M$ could represent the relaxivity of myelin and myelin density, respectively, in Eq. (5). The $R_1$ variation ($\Delta R_1$) within the CC structure can be approximated by the following equation:

$$\Delta R_1 \propto \Delta(R_{1M} \cdot d_M) + \Delta(R_{1Fe} \cdot [\mathrm{Fe}]). \quad (6)$$

Interestingly, the contribution from the second term ($\Delta(R_{1Fe} \cdot [\mathrm{Fe}])$) in the CC is negligible in considering several factors; (1) very low [Fe] in the white matter (WM) compared to the sub-cortical grey matter tissues (Haacke et al. 2005; Langkammer et al. 2010; Hallgren and Sourander 1958); (2) less $R_1$ dependence on [Fe] compared to the $R_2$ dependence in WM (Haacke et al. 2005); and (3) a weak correlation between WM $R_1$ and [Fe] across the brain compared to the relation of $R_2$ or $R_2^*$ with [Fe] (Gelman et al. 2001, 1999). Thus, the contribution of the second term in Eq. (6)

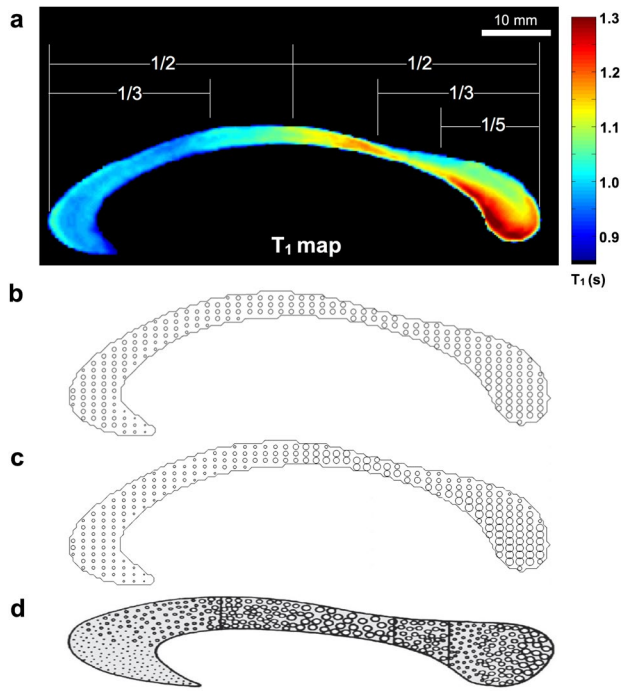


**Fig. 5** In vivo axon diameter maps of the human corpus callosum (**a**–**c**). Each panel represents the subject-averaged $T_1$ relaxometry map (**a**), estimated in vivo axon diameter maps (**b, c**), and manual drawing of axon diameter map reported in the literature (Fig. 1 from the reference Aboitiz and Montiel 2003) (**d**). **c** Drawn after rescaling the axon size distribution for matching the map shown in **d**. There was a qualitatively similar distribution of axon diameter between the in vivo and postmortem estimations: large-size fibers are shown towards the posterior midbody and splenium, while small-size fibers are found in the anterior callosum. Note that all axonal diameter maps provide schematic illustrations by scaling the non-uniform fiber size across the CC, thus, they do not represent the exact ratio of diameters between fibers with varied diameter. **d** Reprinted with the permission from the reference (Aboitiz and Montiel 2003)

becomes negligible and the first term dominates the spatial $R_1$ variation in the human CC tissue and the equation can be simplified to:

$$\Delta R_1(x,y,z) \propto R_{1M} \cdot \Delta d_M(x,y,z). \quad (7)$$

Therefore, the parametric $R_1$ change mainly results from the underlying microstructural properties of myelinated CC tissue and is directly proportional to the myelin density ($d_M$).

The tissue properties of myelinated axons and distribution have been documented with great details by the histology studies. The majority of human CC axons (> 75%) have a diameter range of 0.3–1.0 µm (mean 0.69 µm) (Liewald et al. 2014). Very few myelinated axons in the human brain CC have a small diameter (≤ 0.3 µm) (Waxman and Bennett 1972) and less than 1% of axons have a large diameter (≥ 3 µm) (Aboitiz et al. 1992a). In addition, the thickness of myelin sheath ($t_m$ ~ 0.09 µm) is relatively uniform for the axon population with a diameter range of < 1.0 µm (Aboitiz et al. 1992a; Liewald et al. 2014). Given these factors and parameters reported in the literature, we proposed a simplified model to estimate the relation between axon diameter ($d_a$) and the MWF (Fig. 7c) or the $T_1$ parameter (Fig. 7d) for the human CC. The predicted $T_1$ dependence on the axon diameter is consistent with the reports of histological studies for a similar range of axon diameter (Waxman and Bennett 1972; Ford et al. 2015; Wang et al. 2016). As shown in Fig. 7c, an increase in the axon diameter decreases the MWF (or myelin density) in the human CC, resulting in a lower $R_1$ (or a longer $T_1$) value according to Eq. (7) (Harkins et al. 2016; Wang et al. 2016). Recent in vivo MRI study showed that the MWF in the brain tends to increase in the anterior part of callosum and decrease in the mid-body and splenium (Stikov et al. 2015a). In line with our observation of the high correlate of the callosal $R_1$ with the fiber density (Fig. 4d) and $T_1$ dependence on axon diameter (Fig. 7d), it is likely that the high population of small-size axons in the anterior callosum links high myelin contents and/or increase myelin–water interface, consequentially leading to a short $T_1$ relaxation time. In contrast, the higher population of the large axons located in the posterior midbody and inferior splenium have relatively lower myelin contents and/or reduced myelin–water interfaces, resulting in a long $T_1$ value (Saenz and Fine 2010; Hofer and Frahm 2006; Dougherty et al. 2005b).

We postulate that the mean of callosal $T_1$ value (~ 1.04 s) over the entire mid-sagittal CC slice should correspond to the mean value of the human CC axon diameter [~ 0.69 µm (Liewald et al. 2014)]. Given the $T_1$-based model for axon diameter as depicted in Fig. 7d, the estimated diameter of the superior splenium (S1 in Fig. 3, $T_1 = 1.08$ s) and the inferior splenium (S3 in Fig. 3, $T_1 = 1.25$ s) were 0.72 µm and 0.89 µm, respectively, resulting in up to 19% difference within the splenium. On the other hand, the genu (segment G in Fig. 3, $T_1 = 0.97$ s) has the smallest mean axon diameter of 0.61 µm, resulting in 31% difference compared to the inferior splenium.

Despite the similar pattern of in vivo $T_1$ relaxometry data with the human CC fiber composition of postmortem histology analysis, there are still limited factors to be considered for potential application and interpretation of the $T_1$ relaxometry data for human brain. First, the current image resolution of $T_1$ relaxometry is not sufficient to discriminate the populations of various fiber sizes down to a much fine spatial scale. Instead, we assumed that the $T_1$ value measured from a single MRI voxel represents an averaged quantity from all types of fiber or myelinated axon size. Under this assumption, we aimed to understand the key characteristics of CC subdivisions as investigated in this study. Further improved resolution of callosal $T_1$ image is needed to provide a more precise estimation

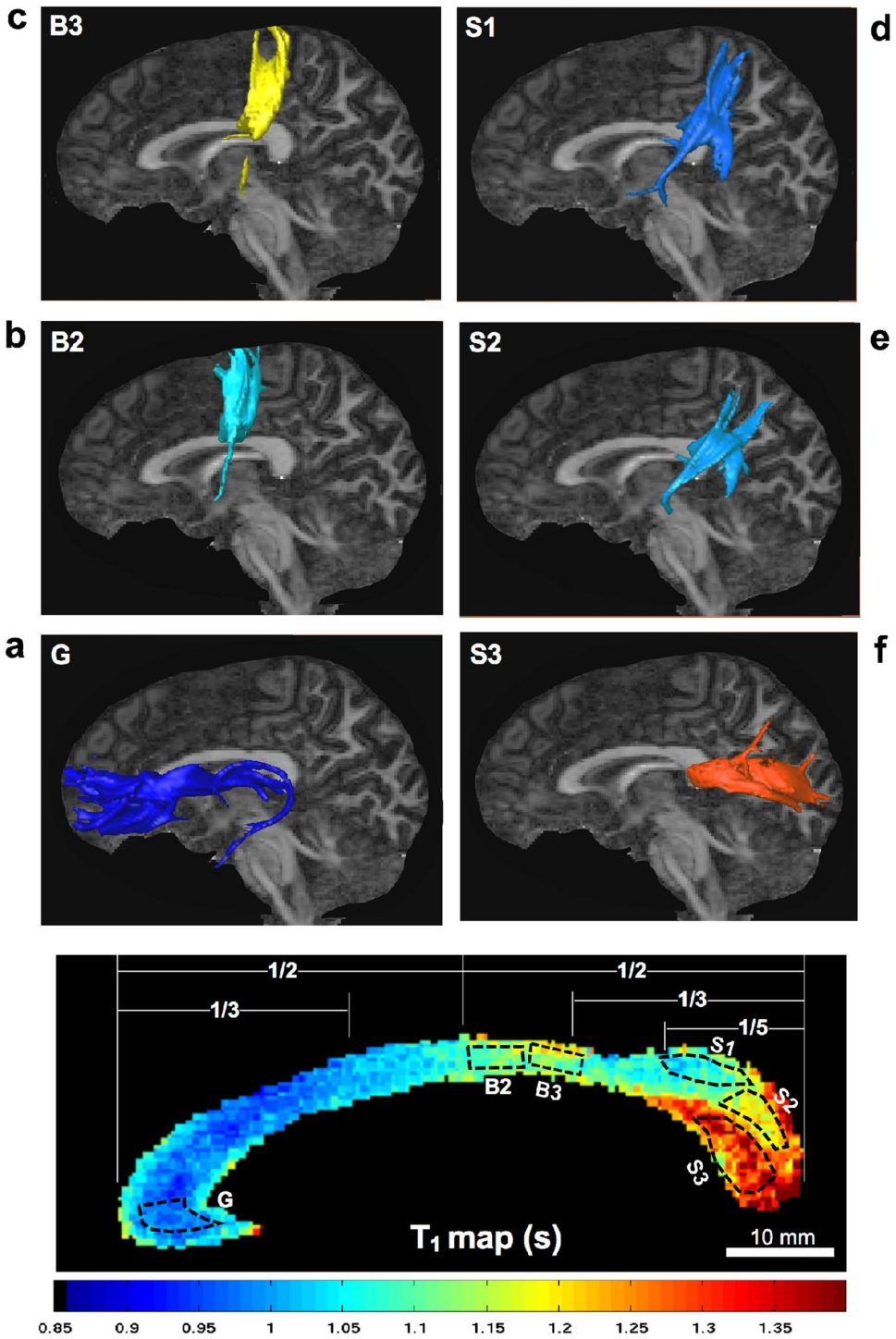


**Fig. 6** Diffusion tractography for the human callosal fibers. The callosal fibers from each seeding region of interest (ROI, the dotted areas), which was delineated from the callosal $T_1$ relaxometry map (panel at the bottom), were connected to the structurally projected cortical areas: **a** ROI G to prefrontal lobe; **b** ROI B2 to motor cortex; **c** ROI B3 to sensory cortex; **d, e** ROIs S1 and S2 to parietal–temporal lobes; and **f** ROI S3 to occipital lobe

of the fine fiber composition and distinct features of the human CC in healthy subjects. Secondly, the proposed model for axon diameter was used to visualize the key feature of callosal fiber diameter under the assumption of major contribution of MWF to the $T_1$ relaxation changes. Considering the complexity of fiber structure of the CC, this simplified model might underestimate the other mechanisms responsible for $T_1$ changes via the interactions with intracellular and extracellular water contents.

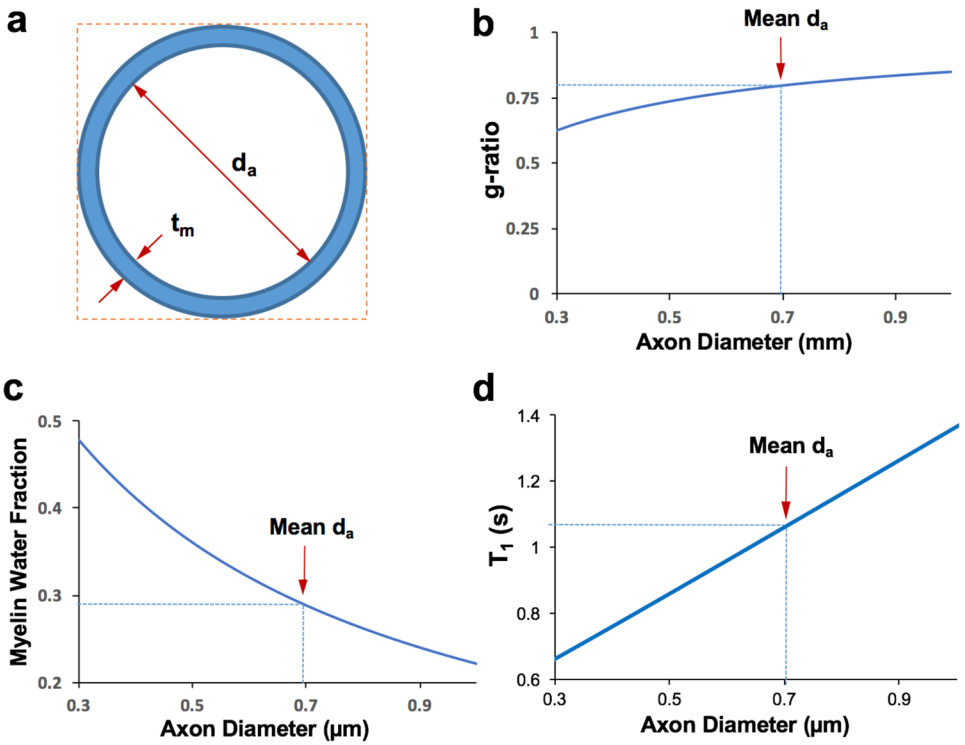


**Fig. 7** In vivo model for myelinated axonal diameter. **a** A simplified model of myelinated axon diameter under assumption of an approximation of constant myelin sheath thickness ($t_m$ ~ 0.09 μm). **b** The estimated microstructure *g*-ratio [$=d_a/(d_a + 2 \times t_m)$], where $d_a$ is the axon diameter, and its mean value is 0.69 μm (pointed by the red arrow) in the human CC (Aboitiz et al. 1992b; Liewald et al. 2014). **c** The estimated myelin water fraction (MWF $= \frac{\pi}{4}(1 - \text{g-ratio}^2)$ or $\frac{\pi}{4}(1 - (d_a/(d_a + 2 \times t_m)^2))$ as a function of axon diameter. **d** The estimated relation between $T_1$ and MWF ($T_1 = 0.291/\text{MWF} + 0.05$)

## Conclusions

In summary, this study suggests that the CC characterization using the high-resolution $T_1$ relaxometry mapping method has the potential to robustly assess and quantify the microstructural properties, which links its functional connectivity in the human brain. Therefore, this $T_1$ imaging approach could be a highly useful neuroimaging tool for studying basic brain function and development, neural plasticity and aging process in healthy population.

**Acknowledgements** This work was supported by NIH Grants RO1 NS070839 and MH111413; R24 MH106049, S10 RR026783, U01 EB026978, P41 EB015894, and P30NS076408 and the W.M. Keck Foundation.

## Compliance with ethical standards

**Ethical approval** All procedures performed in the studies involving human participants were in accordance with the ethical standards of the institutional and/or national research committee and with the 1964 Helsinki declaration and its later amendments or comparable ethical standards.

**Conflict of interest** The authors declare no conflict of interest.

## References

Aboitiz F, Montiel J (2003) One hundred million years of interhemispheric communication: the history of the corpus callosum. Braz J Med Biol Res 36 (4):409–420

Aboitiz F, Scheibel AB, Fisher RS, Zaidel E (1992a) Fiber composition of the human corpus callosum. Brain Res 598(1–2):143–153

Aboitiz F, Scheibel AB, Fisher RS, Zaidel E (1992b) Individual differences in brain asymmetries and fiber composition in the human corpus callosum. Brain Res 598(1–2):154–161

Alexander DC, Hubbard PL, Hall MG, Moore EA, Ptito M, Parker GJ, Dyrby TB (2010) Orientationally invariant indices of axon diameter and density from diffusion MRI. Neuroimage 52(4):1374–1389. https://doi.org/10.1016/j.neuroimage.2010.05.043

Andersson JL, Skare S, Ashburner J (2003) How to correct susceptibility distortions in spin-echo echo-planar images: application to diffusion tensor imaging. Neuroimage 20(2):870–888. https://doi.org/10.1016/S1053-8119(03)00336-7

Assaf Y, Blumenfeld-Katzir T, Yovel Y, Basser PJ (2008) AxCaliber: a method for measuring axon diameter distribution from diffusion MRI. Magn Reson Med 59(6):1347–1354. https://doi.org/10.1002/mrm.21577

Assaf Y, Alexander DC, Jones DK, Bizzi A, Behrens TE, Clark CA, Cohen Y, Dyrby TB, Huppi PS, Knoesche TR, Lebihan D, Parker GJ, Poupon C, consortium C, Anaby D, Anwander A, Bar L, Barazany D, Blumenfeld-Katzir T, De-Santis S, Duclap D, Figini M, Fischi E, Guevara P, Hubbard P, Hofstetter S, Jbabdi S, Kunz N, Lazeyras F, Lebois A, Liptrot MG, Lundell H, Mangin JF, Dominguez DM, Morozov D, Schreiber J, Seunarine K, Nava S, Poupon C, Riffert T, Sasson E, Schmitt B, Shemesh N, Sotiropoulos SN, Tavor I, Zhang HG, Zhou FL (2013) The CONNECT project: combining macro- and micro-structure. Neuroimage 80:273–282. https://doi.org/10.1016/j.neuroimage.2013.05.055

Behrens TE, Berg HJ, Jbabdi S, Rushworth MF, Woolrich MW (2007) Probabilistic diffusion tractography with multiple fibre

orientations: what can we gain? Neuroimage 34(1):144–155. https://doi.org/10.1016/j.neuroimage.2006.09.018
Berlucchi G (1972) Anatomical and physiological aspects of visual functions of corpus callosum. Brain Res 37(2):371–392
Björnholm L, Nikkinen J, Kiviniemi V, Nordström T, Niemelä S, Drakesmith M, Evans JC, Pike GB, Veijola J, Paus T (2017) Structural properties of the human corpus callosum: multimodal assessment and sex differences. Neuroimage 152:108–118. https://doi.org/10.1016/j.neuroimage.2017.02.056
Budd JM, Kisvarday ZF (2012) Communication and wiring in the cortical connectome. Front Neuroanat 6:42. https://doi.org/10.3389/fnana.2012.00042
Callaghan PT, Eccles CD, Xia Y (1988) NMR microscopy of dynamic displacements: k-space and q-space imaging. J Phys E Sci Instrum 21(8):820
Caminiti R, Ghaziri H, Galuske R, Hof PR, Innocenti GM (2009) Evolution amplified processing with temporally dispersed slow neuronal connectivity in primates. Proc Natl Acad Sci USA 106(46):19551–19556. https://doi.org/10.1073/pnas.0907655106
Caminiti R, Carducci F, Piervincenzi C, Battaglia-Mayer A, Confalone G, Visco-Comandini F, Pantano P, Innocenti GM (2013) Diameter, length, speed, and conduction delay of callosal axons in macaque monkeys and humans: comparing data from histology and magnetic resonance imaging diffusion tractography. J Neurosci 33(36):14501–14511. https://doi.org/10.1523/JNEUROSCI.0761-13.2013
Chenevert TL, Brunberg JA, Pipe JG (1990) Anisotropic diffusion in human white matter: demonstration with MR techniques in vivo. Radiology 177(2):401–405. https://doi.org/10.1148/radiology.177.2.2217776
de Lacoste MC, Kirkpatrick JB, Ross ED (1985) Topography of the human corpus callosum. J Neuropathol Exp Neurol 44(6):578–591
Dougherty RF, Ben-Shachar M, Bammer R, Brewer AA, Wandell BA (2005a) Functional organization of human occipital-callosal fiber tracts. Proc Natl Acad Sci USA 102(20):7350–7355. https://doi.org/10.1073/pnas.0500003102
Dougherty RF, Ben-Shachar M, Deutsch G, Potanina P, Bammer R, Wandell BA (2005b) Occipital–callosal pathways in children: validation and atlas development. Ann N Y Acad Sci 1064:98–112. https://doi.org/10.1196/annals.1340.017
Fabri M, Pierpaoli C, Barbaresi P, Polonara G (2014) Functional topography of the corpus callosum investigated by DTI and fMRI. World J Radiol 6(12):895–906. https://doi.org/10.4329/wjr.v6.i12.895
Ford MC, Alexandrova O, Cossell L, Stange-Marten A, Sinclair J, Kopp-Scheinpflug C, Pecka M, Attwell D, Grothe B (2015) Tuning of Ranvier node and internode properties in myelinated axons to adjust action potential timing. Nat Commun 6:8073. https://doi.org/10.1038/ncomms9073
Garwood M, DelaBarre L (2001) The return of the frequency sweep: designing adiabatic pulses for contemporary NMR. J Magn Reson 153(2):155–177. https://doi.org/10.1006/jmre.2001.2340
Gelman N, Gorell JM, Barker PB, Savage RM, Spickler EM, Windham JP, Knight RA (1999) MR imaging of human brain at 3.0 T: preliminary report on transverse relaxation rates and relation to estimated iron content. Radiology 210(3):759–767. https://doi.org/10.1148/radiology.210.3.r99fe41759
Gelman N, Ewing JR, Gorell JM, Spickler EM, Solomon EG (2001) Interregional variation of longitudinal relaxation rates in human brain at 3.0 T: relation to estimated iron and water contents. Magn Reson Med 45(1):71–79
Genc S, Malpas CB, Ball G, Silk TJ, Seal ML (2018) Age, sex, and puberty related development of the corpus callosum: a multi-technique diffusion MRI study. Brain Struct Funct 223(6):2753–2765. https://doi.org/10.1007/s00429-018-1658-5
Good CD, Johnsrude IS, Ashburner J, Henson RN, Friston KJ, Frackowiak RS (2001) A voxel-based morphometric study of ageing in 465 normal adult human brains. Neuroimage 14(1 Pt 1):21–36
Haacke EM, Cheng NY, House MJ, Liu Q, Neelavalli J, Ogg RJ, Khan A, Ayaz M, Kirsch W, Obenaus A (2005) Imaging iron stores in the brain using magnetic resonance imaging. Magn Reson Imaging 23(1):1–25. https://doi.org/10.1016/j.mri.2004.10.001
Hallgren B, Sourander P (1958) The effect of age on the non-haemin iron in the human brain. J Neurochem 3(1):41–51. doi:https://doi.org/10.1111/j.1471-4159.1958.tb12607.x
Hargreaves BA, Cunningham CH, Nishimura DG, Conolly SM (2004) Variable-rate selective excitation for rapid MRI sequences. Magn Reson Med 52(3):590–597. https://doi.org/10.1002/mrm.20168
Harkins KD, Xu J, Dula AN, Li K, Valentine WM, Gochberg DF, Gore JC, Does MD (2016) The microstructural correlates of $T_1$ in white matter. Magn Reson Med 75(3):1341–1345. https://doi.org/10.1002/mrm.25709
Harkins Kevin D, Xu J, Dula Adrienne N, Li K, Valentine William M, Gochberg Daniel F, Gore John C, Does Mark D (2016) The microstructural correlates of $T_1$ in white matter. Magn Reson Med 75(3):1341–1345. https://doi.org/10.1002/mrm.25709 doi
Hofer S, Frahm J (2006) Topography of the human corpus callosum revisited—comprehensive fiber tractography using diffusion tensor magnetic resonance imaging. Neuroimage 32(3):989–994. https://doi.org/10.1016/j.neuroimage.2006.05.044
Hofer S, Wang X, Roeloffs V, Frahm J (2015) Single-shot $T_1$ mapping of the corpus callosum: a rapid characterization of fiber bundle anatomy. Front Neuroanat 9:57. https://doi.org/10.3389/fnana.2015.00057
Huang H, Zhang J, Jiang H, Wakana S, Poetscher L, Miller MI, van Zijl PC, Hillis AE, Wytik R, Mori S (2005) DTI tractography based parcellation of white matter: application to the mid-sagittal morphology of corpus callosum. Neuroimage 26(1):195–205. https://doi.org/10.1016/j.neuroimage.2005.01.019
Innocenti GM, Caminiti R, Hof PR (2010) Fiber composition in the planum temporale sector of the corpus callosum in chimpanzee and human. Brain Struct Funct 215(2):123–128. https://doi.org/10.1007/s00429-010-0274-9
Jensen JH, Helpern JA, Ramani A, Lu H, Kaczynski K (2005) Diffusional kurtosis imaging: the quantification of non-Gaussian water diffusion by means of magnetic resonance imaging. Magn Reson Med 53(6):1432–1440. https://doi.org/10.1002/mrm.20508
Kontis D, Catani M, Cuddy M, Walshe M, Nosarti C, Jones D, Wyatt J, Rifkin L, Murray R, Allin M (2009) Diffusion tensor MRI of the corpus callosum and cognitive function in adults born preterm. Neuroreport 20(4):424–428. https://doi.org/10.1097/WNR.0b013e328325a8f9
Lamantia AS, Rakic P (1990) Cytological and quantitative characteristics of four cerebral commissures in the rhesus monkey. J Comp Neurol 291(4):520–537. https://doi.org/10.1002/cne.902910404
Langkammer C, Krebs N, Goessler W, Scheurer E, Ebner F, Yen K, Fazekas F, Ropele S (2010) Quantitative MR imaging of brain iron: a postmortem validation study. Radiology 257(2):455–462. https://doi.org/10.1148/radiol.10100495
Le Bihan D, Breton E, Lallemand D, Grenier P, Cabanis E, Laval-Jeantet M (1986) MR imaging of intravoxel incoherent motions: application to diffusion and perfusion in neurologic disorders. Radiology 161(2):401–407. https://doi.org/10.1148/radiology.161.2.3763909
Lee B-Y, Zhu X-H, Li X, Chen W (2014) Quantitative assessment of microstructure properties of human corpus callosum using parametric $T_1$ and Myelin imaging. Proc Intl Soc Mag Reson Med 2014:32–36
Li X, Bolan PJ, Ugurbil K, Metzger GJ (2015) Measuring renal tissue relaxation times at 7 T. NMR Biomed 28(1):63–69. https://doi.org/10.1002/nbm.3195

Liewald D, Miller R, Logothetis N, Wagner HJ, Schuz A (2014) Distribution of axon diameters in cortical white matter: an electron-microscopic study on three human brains and a macaque. Biol Cybern 108(5):541–557. https://doi.org/10.1007/s00422-014-0626-2

Moeller S, Yacoub E, Olman CA, Auerbach E, Strupp J, Harel N, Uğurbil K (2010) Multiband multislice GE-EPI at 7 T, with 16-fold acceleration using partial parallel imaging with application to high spatial and temporal whole-brain fMRI. Magn Reson Med 63(5):1144–1153. https://doi.org/10.1002/mrm.22361

Myers RE (1959) Localization of function in the corpus callosum. Visual gnostic transfer. Arch Neurol 1:74–77

Narr KL, Thompson PM, Sharma T, Moussai J, Cannestra AF, Toga AW (2000) Mapping morphology of the corpus callosum in schizophrenia. Cereb Cortex 10(1):40–49

Park HJ, Kim JJ, Lee SK, Seok JH, Chun J, Kim DI, Lee JD (2008) Corpus callosal connection mapping using cortical gray matter parcellation and DT-MRI. Hum Brain Mapp 29(5):503–516. https://doi.org/10.1002/hbm.20314

Payne BR (1990) Function of the corpus callosum in the representation of the visual field in cat visual cortex. Vis Neurosci 5(2):205–211

Putnam MC, Steven MS, Doron KW, Riggall AC, Gazzaniga MS (2010) Cortical projection topography of the human splenium: hemispheric asymmetry and individual differences. J Cogn Neurosci 22(8):1662–1669. https://doi.org/10.1162/jocn.2009.21290

Rooney WD, Johnson G, Li X, Cohen ER, Kim SG, Ugurbil K, Springer CS Jr (2007) Magnetic field and tissue dependencies of human brain longitudinal $^{1}H_2O$ relaxation in vivo. Magn Reson Med 57(2):308–318. https://doi.org/10.1002/mrm.21122

Saenz M, Fine I (2010) Topographic organization of V1 projections through the corpus callosum in humans. Neuroimage 52(4):1224–1229. https://doi.org/10.1016/j.neuroimage.2010.05.060

Sereno MI, Lutti A, Weiskopf N, Dick F (2013) Mapping the human cortical surface by combining quantitative T(1) with retinotopy. Cereb Cortex 23(9):2261–2268. https://doi.org/10.1093/cercor/bhs213

Sigalovsky IS, Fischl B, Melcher JR (2006) Mapping an intrinsic MR property of gray matter in auditory cortex of living humans: a possible marker for primary cortex and hemispheric differences. Neuroimage 32(4):1524–1537. https://doi.org/10.1016/j.neuroimage.2006.05.023

Sisti HM, Geurts M, Gooijers J, Heitger MH, Caeyenberghs K, Beets IA, Serbruyns L, Leemans A, Swinnen SP (2012) Microstructural organization of corpus callosum projections to prefrontal cortex predicts bimanual motor learning. Learn Mem 19(8):351–357. https://doi.org/10.1101/lm.026534.112

Sotiropoulos SN, Jbabdi S, Xu J, Andersson JL, Moeller S, Auerbach EJ, Glasser MF, Hernandez M, Sapiro G, Jenkinson M, Feinberg DA, Yacoub E, Lenglet C, Van Essen DC, Ugurbil K, Behrens TE, Consortium WU-MH (2013) Advances in diffusion MRI acquisition and processing in the Human Connectome Project. Neuroimage 80:125–143. https://doi.org/10.1016/j.neuroimage.2013.05.057

Stikov N, Perry LM, Mezer A, Rykhlevskaia E, Wandell BA, Pauly JM, Dougherty RF (2011) Bound pool fractions complement diffusion measures to describe white matter micro and macrostructure. Neuroimage 54(2):1112–1121. https://doi.org/10.1016/j.neuroimage.2010.08.068

Stikov N, Campbell JS, Stroh T, Lavelee M, Frey S, Novek J, Nuara S, Ho MK, Bedell BJ, Dougherty RF, Leppert IR, Boudreau M, Narayanan S, Duval T, Cohen-Adad J, Picard PA, Gasecka A, Cote D, Pike GB (2015a) In vivo histology of the myelin *g*-ratio with magnetic resonance imaging. Neuroimage 118:397–405. https://doi.org/10.1016/j.neuroimage.2015.05.023

Stikov N, Campbell JS, Stroh T, Lavelee M, Frey S, Novek J, Nuara S, Ho MK, Bedell BJ, Dougherty RF, Leppert IR, Boudreau M, Narayanan S, Duval T, Cohen-Adad J, Picard PA, Gasecka A, Cote D, Pike GB (2015b) Quantitative analysis of the myelin *g*-ratio from electron microscopy images of the macaque corpus callosum. Data Brief 4:368–373. https://doi.org/10.1016/j.dib.2015.05.019

Stuber C, Morawski M, Schafer A, Labadie C, Wahnert M, Leuze C, Streicher M, Barapatre N, Reimann K, Geyer S, Spemann D, Turner R (2014) Myelin and iron concentration in the human brain: a quantitative study of MRI contrast. Neuroimage 93 Pt 1:95–106. https://doi.org/10.1016/j.neuroimage.2014.02.026

Thapaliya K, Vegh V, Bollmann S, Barth M (2017) Assessment of microstructural signal compartments across the corpus callosum using multi-echo gradient recalled echo at 7 T. Neuroimage. https://doi.org/10.1016/j.neuroimage.2017.11.029

Tomasi S, Caminiti R, Innocenti GM (2012) Areal differences in diameter and length of corticofugal projections. Cereb Cortex 22(6):1463–1472. https://doi.org/10.1093/cercor/bhs011

Tuch DS, Reese TG, Wiegell MR, Makris N, Belliveau JW, Wedeen VJ (2002) High angular resolution diffusion imaging reveals intravoxel white matter fiber heterogeneity. Magn Reson Med 48(4):577–582. https://doi.org/10.1002/mrm.10268

Ugurbil K, Xu J, Auerbach EJ, Moeller S, Vu AT, Duarte-Carvajalino JM, Lenglet C, Wu X, Schmitter S, Van de Moortele PF, Strupp J, Sapiro G, De Martino F, Wang D, Harel N, Garwood M, Chen L, Feinberg DA, Smith SM, Miller KL, Sotiropoulos SN, Jbabdi S, Andersson JL, Behrens TE, Glasser MF, Van Essen DC, Yacoub E, Consortium WU-MH (2013) Pushing spatial and temporal resolution for functional and diffusion MRI in the Human Connectome Project. Neuroimage 80:80–104. https://doi.org/10.1016/j.neuroimage.2013.05.012

Vu AT, Auerbach E, Lenglet C, Moeller S, Sotiropoulos SN, Jbabdi S, Andersson J, Yacoub E, Ugurbil K (2015) High resolution whole brain diffusion imaging at 7T for the Human Connectome Project. Neuroimage 122:318–331. https://doi.org/10.1016/j.neuroimage.2015.08.004

Wahl M, Lauterbach-Soon B, Hattingen E, Jung P, Singer O, Volz S, Klein JC, Steinmetz H, Ziemann U (2007) Human motor corpus callosum: topography, somatotopy, and link between microstructure and function. J Neurosci 27(45):12132–12138. https://doi.org/10.1523/JNEUROSCI.2320-07.2007

Wang X, Zhu XH, Zhang Y, Chen W (2016) In vivo parametric $T_1/R_1$ imaging correlation with myelin density and microstructure properties of rat corpus callosum. In: Proceedings of international society for magnetic resonance in medicine, p 1465

Waxman SG, Bennett MV (1972) Relative conduction velocities of small myelinated and non-myelinated fibres in the central nervous system. Nat New Biol 238(85):217–219

Witelson SF (1989) Hand and sex differences in the isthmus and genu of the human corpus callosum. A postmortem morphological study. Brain 112(Pt 3):799–835

Wright PJ, Mougin OE, Totman JJ, Peters AM, Brookes MJ, Coxon R, Morris PE, Clemence M, Francis ST, Bowtell RW, Gowland PA (2008) Water proton $T_1$ measurements in brain tissue at 7, 3, and 1.5 T using IR-EPI, IR-TSE, and MPRAGE: results and optimization. MAGMA 21(1–2):121–130. https://doi.org/10.1007/s10334-008-0104-8

Yarnykh VL (2007) Actual flip-angle imaging in the pulsed steady state: a method for rapid three-dimensional mapping of the transmitted radiofrequency field. Magn Reson Med 57(1):192–200. https://doi.org/10.1002/mrm.21120

Zhang H, Hubbard PL, Parker GJ, Alexander DC (2011) Axon diameter mapping in the presence of orientation dispersion with diffusion MRI. Neuroimage 56(3):1301–1315. https://doi.org/10.1016/j.neuroimage.2011.01.084